Genetically tailored magnetosomes used as MRI probe for molecular imaging of brain tumor

M. Boucher, F. Geffroy, S. Prévéral, L. Bellanger, E. Selingue, Géraldine Adryanczyk-Perrier, M. Pean, Christopher T. Lefèvre, D Pignol, N. Ginet, et al.

Genetically tailored magnetosomes used as MRI probe for molecular imaging of brain tumor

M.Boucher[a], F.Geffroy[a], S.Prévéral[bcd], L.Bellanger[e], E.Selingue[a], G.AdryanczykPerrier[bcd], M.Péan[bcd], C.T.Lefèvre[bcd], D.Pignol[bcd], N.Ginet[bcdf], S.Mériaux[a]

a UNIRS, CEA/DRF/I^{2}BM/NeuroSpin, CEA Saclay, Gif-sur-Yvette, France
b LBC, CEA/DRF/BIAM, CEA Cadarache, Saint-Paul-lez-Durance, France
c UMR 7265, Centre National de Recherche Scientifique, Saint-Paul-lez-Durance, France
d Aix Marseille Université, Saint-Paul-lez-Durance, France
e LI2D, CEA/DRF/IBITEC-S/SPI, CEA Marcoule, Bagnols-sur-Cèze, France
f Aix Marseille Université, CNRS, Laboratoire de Chimie Bactérienne, Marseille, France

Abstract

We investigate here the potential of single step production of genetically engineeredmagnetosomes, bacterial biogenic iron-oxide nanoparticles embedded in a lipid vesicle, as a new tailorable magnetic resonance molecular imaging probe. We demonstrate *in vitro* the specific binding and the significant internalization into U87 cells of magnetosomes decorated with RGD peptide. After injection at the tail vein of glioblastoma-bearing mice, we evidence in the first 2 h the rapid accumulation of both unlabeled and functionalized magnetosomes inside the tumor by Enhanced Permeability and Retention effects. 24 h after the injection, a specific enhancement of the tumor contrast is observed on MR images only for RGD-labeled magnetosomes. *Post mortem* acquisition of histological data confirms MRI results with more magnetosomes found into the tumor treated with functionalized magnetosomes. This work establishes the first proof-of-concept of a successful bio-integrated production of molecular imaging probe for MRI.

1. Introduction

The rise of precision medicine, which aims at tailoring personal medical treatments and therapies but also human well-being monitoring, is highly supported worldwide by public research policies. However, while medical imaging, such as X rays, echography, Positron Emission Tomography (PET) and MRI (Magnetic Resonance Imaging), is daily used to get anatomical and functional information, subcellular and even molecular detection of prognostic and diagnostic physiological markers is striving to reach the patient's bed. In this context, molecular imaging aims at overcoming the lack of specificity and sensitivity of conventional imaging strategies to reveal molecular or cellular phenomenon of medical interest in the less invasive manner. Unraveling such information enables to diagnose diseases at earlier stage and tailor therapeutic strategies to patient's variability.

Molecular imaging requires in many cases the development of specific functionalized contrast agents to reveal molecular or cellular phenomenon with dedicated imaging modality. Currently, the most advanced modality for this purpose is PET imaging [1], with a high

sensitivity for biomarkers detection, but a low spatial resolution and the use of radioactive compounds as the main drawbacks. Fluorescence imaging is also very promising since it exhibits a very good sensitivity. However, the poor penetration and complex diffusion of photons in living tissues currently restrains its use mainly to intraoperative applications. On the contrary, MRI suffers from poor sensitivity but offers very high spatial resolution [2], does not rely on radionuclides and can non-invasively provide in-depth information. Its sensitivity can yet be enhanced firstly by increasing the intensity of static magnetic field, secondly by improving the detection sensitivity of radiofrequency coils, and thirdly by optimizing the contrasting part of molecular imaging probes. In particular, iron-oxide nanoparticles are well studied MRI contrast agents [3]. Their contrasting properties can be tuned by changing size and/or shape, or even by doping them with other atoms [3–5]. In addition, functionalization of the probe surface by suitable ligands can confer selectivity for the targeted biomarker, tissue or organ. Additional probe engineering for drug delivery and other therapeutic effects can convert these vectors into theranostic agents. In this context, functionalization of iron-oxide nanoparticles using different strategies, such as antibodies, aptamers, cell penetrating peptides or drugs, is investigated in a variety of applications, in cancer or inflammation diagnosis for example [4,5]. Thanks to their metallic core, such agents can also play a key role in cell tracking after transplantation [6], and can also locally deliver thermal energy for thermoablation therapies [7]. However, since the mineral core of chemically synthesized iron-oxide nanoparticles is not dispersible in biological fluids, various coating strategies have been developed to ensure biocompatibility with additional properties such as vascular retention/clearance, stealthiness, anchoring points for targeting ligand and even encapsulation of active molecules [8]. These engineered molecular probes result from a series of multiple manufacturing steps, each requiring separate optimization with their technical difficulties and cost, thus impeding their wide use.

Recently, studies demonstrated the great interest of biogenic gas nanostructures as potential molecular reporters for ultrasonic imaging [9], and for labeling and quantifying gene expression by MRI [10]. Likewise, in this study, we explored a new alternative path, based on the use of living organisms, to produce engineered high efficiency molecular imaging probes. We focused on the potential of magnetosomes, biomineralized iron-oxide nanoparticles naturally coated by a biological membrane and produced by magnetotactic bacteria. Magnetosomes size and shape are strain dependent [11] and their iron-oxide core presents a very good crystallinity along with a narrow size distribution [12], and is bigger than the one of conventional chemical iron-oxide nanoparticles [3,12]. Thus these mono-domain magnetite nanoparticles exhibit permanent magnetization, and are then naturally awarded with high contrasting properties for MRI [13–17]. Moreover, magnetosomes are naturally biocompatible because of the lipid bilayer surrounding the iron-oxide core [18,19], which corroborates their potential as MRI contrast agent [17,20–22]. Furthermore, we previously evidenced that magnetosomes easily purified from bacterial cultures can be used as *in vivo* contrast agent, allowing the visualization of mouse brain angiograms after systemic injection [17]. Magnetosomes can also be genetically functionalized with peptides or proteins using a

translational fusion between the gene coding for an abundant protein specific to the magnetosome membrane, like *mamC*[23], and a gene encoding the targeting ligand. The decoration is thus naturally sorted to the membrane leading to a functionalized magnetosome [14,24].

Hence, this study establishes the first proof-of-concept of functionalized MRI contrast agent produced in a single step from genetically modified magnetotactic bacteria, in order to perform *in vivo* MR-based molecular imaging of brain tumor in a mouse model of glioblastoma. Molecular imaging of brain tumor is particularly valuable since it could help performing early diagnosis, as well as monitoring treatment efficiency, and might even be coupled with therapy [4,25,26]. To date, brain tumor targeting has been successfully achieved through the EPR (Enhanced Permeability and Retention) effect [27] (a passive targeting due to the leakiness of tumor blood vessels), or by active targeting of angiogenesis molecular biomarkers [25], such as $\alpha_v\beta_3$ integrins overexpressed by tumor cells and in new vascular epithelium [28], and involved in development of new blood vessels and cell motility[29,30]. The $\alpha_v\beta_3$ integrin can be targeted *in vivo* using RGD (Arginine, Glycine, Aspartic acid) peptide, which binding efficiency has been demonstrated by several studies [26,28,31].

Thus, we decorated the outer surface of magnetosomes with the RGD peptide by genetically manipulating a *Magnetospirillum magneticum* AMB-1 strain. To confirm the proper functionalization of magnetosomes, we used the Venus protein as a fluorescent reporter. We characterized *in vitro* the specific affinity and consecutive internalization of RGD-labeled magnetosomes into U87 glioblastoma cell culturesand confirmed their MRI contrasting properties. We injected RGD-labeled and unlabeled magnetosomes at the tail vein of glioblastoma-bearing mice, and acquired longitudinal series of high spatial resolution MR images. We evidenced the strong accumulation of magnetosomes inside the tumor by EPR effect that persisted long after the complete washout of the nanoparticles from the blood vasculature. Furthermore data analysis revealed a specific enhancement of the tumor contrast on MR images for the RGD-labeled magnetosomes compared to the unlabeled ones. Finally, we cross-validated MRI results with *post mortem* acquisition of histological data, and provided the first evidence that the affinity and contrast properties of our RGD-functionalized magnetosomes were suitable for *in vivo* MR-based molecular imaging of our glioblastoma mouse model.

2. Materials and methods

2.1. *Magnetotactic bacteria cultivation and magnetosomes production*

Genetically modified *Magnetospirillum magneticum* AMB-1 [32] cells were anaerobically grown in 7 L bioreactors (Labfors 5, INFORS HT) until late exponential phase. The defined culture medium for anaerobic growth was modified from Murat et al. [33] by increasing the nitrate concentration up to 10 mM. Bacterial cells were harvested by centrifugation and frozen pellets were stored at −20 °C until use. Typically purified magnetosomes suspensions

were prepared using the protocol described in Mériaux et al. [17]. 4 g pellets were obtained by resuspending the cells in 10 mL of Buffer 1 (20 mM HEPES, 1 mM EDTA, 8% glycerol, 0.9% NaCl, pH 7.5). Bacterial cells were disrupted 3 times with a French press (1200 psi). Magnetosomes were magnetically purified with a MACSiMAG™ separator (Miltenyi Biotec). The magnetic nanoparticles were then washed and magnetically purified 10 times in 10 mL of Buffer 2 (20 mM HEPES, 8% glycerol, 0.9% NaCl, pH 7.5). Magnetosomes were finally resuspended in 200 µL of Buffer 3 (20 mM HEPES, 8% glycerol, pH 7.5), flash-frozen in liquid nitrogen and stored at −80 °C. Throughout the purification process, we verified the functionalization by recording fluorescence emission spectra on an INFINTE® 200 microplate reader from TECAN, in 96 wells white microplates with the excitation wavelength set at 490 nm. The iron content was determined by Inductively Coupled Plasma Atomic Emission Spectroscopy(ICP-AES) after mineralization in the presence of nitric acid and overnight incubation at 80 °C. Magnetosomes were then thawed and diluted at an iron concentration of 54 mM (3 g/L), and reconditioned in 180 µL readily injectable doses stored at −80 °C. We used Venus fluorescence to verify that this thawing/freezing cycle does not affect magnetosomes functionalization. Magnetosome protein content was determined according to the modified Bradford method (Coo Protein Assay, INTERCHIM) after incubation in 0.1 M *NaOH for 30 min at 60 °C.*

2.2. Genetic modification of Magnetospirillum magneticum AMB-1

In order to express at the magnetosomes surface the Venus protein – a Yellow Fluorescent Protein (YFP) being a variant of the Green Fluorescent Protein – bearing or not the RGD peptide, we designed two plasmids (pMamC-Venus and pMamC-VenusRGD) bearing the translational fusion between *mamC* and *venus* (or *venusRGD*) genes. We used as a scaffold the pMamC-Opd plasmid previously used to functionalize the magnetosomes surface with the organophosphohydrolase (Opd) from *Flavobacterium sp.* ATCC 27551 [24]. The *opd* gene was excised by restriction digestion (BamHI and SacI); then the *venus* or *venusRGD* PCR products were obtained with 2 different primers pairs (Primers #1 and #2 for *venus*, Primers #1 and #3 for *venusRGD*, see Table 1) from a local plasmid containing the *venus* gene. After double enzymatic digestion with BamHI and SacI, the PCR products were then cloned at the corresponding sites into the previously digested plasmid. In the pMamC-VenusRGD vector, the 3′ extremity of the *mamc::venusRGD* chimeric genecodes for an 11 aminoacids peptide (ACDC**RGD**CFCG) bearing the RGD motif. *Magnetospirillum magneticum* AMB-1 wild-type strain was transformed by conjugation as described by Ginet et al. [24].

Table 1. List of primers used in this study.

Primer #	Sequence (5′ -> 3′)
1	TATAGGATCCGTGAGCAAGGGCGAGGAG
2	TATAGAGCTCTTACTTGTACAGCTCGTC
3	TATAGAGCTCTTAGCCACAAAAACAATCGCCTCTACAATCACAAGCCTTGTACAGCTCGTC

2.3. *Western blot analysis*

Magnetosome proteins were separated by SDS-PAGE on 12% Bis-Tris gels (10 µg protein loaded in each well), then transferred onto a nitrocellulose membrane. Membrane blocking and primary anti-GFP antibody incubation (1/5000 dilution) were done according to the manufacturer protocol (Living Colors® A.v. Monoclonal Antibody JL-8, Clontech). The secondary anti-mouse IgG-Peroxidase antibody incubation was performed according to the manufacturer recommendation (Sigma-Aldrich). The chemiluminescence signal was obtained with the SuperSignal™ West Pico Chemiluminescent Substrate (ThermoFisher) and imaged with a G:BOX imaging system (Syngene).

2.4. *Transmission electron microscopy*

For TEM imaging, 10 µL deposits of diluted magnetosomes suspension were allowed to sediment for 1 min onto 200 mesh copper grids covered by a formvar-carbon film. After removal of the liquid with Kimwipe paper, digital electron micrographs were recorded with a Tecnai™ G2 BioTWIN transmission electron microscope (FEI Company) at 100 kV acceleration voltage.

2.5. *Confocal microscopy*

Confocal microscopy images presented in Fig. 1a were collected on a Zeiss LSM880 confocal microscope equipped with an Airyscan detector (Carl Zeiss) using a Plan-Apochromat 63x/1.40 Oil DIC M27 objective. YFP was excited with a blue argon ion laser (514 nm), and emitted light was recorded between 520 and 640 nm. DIC (differential interference contrast) images were acquired simultaneously with the fluorescence images using the transmitted light detector. Images were processed using Zen 2 software (Carl Zeiss, blue edition).

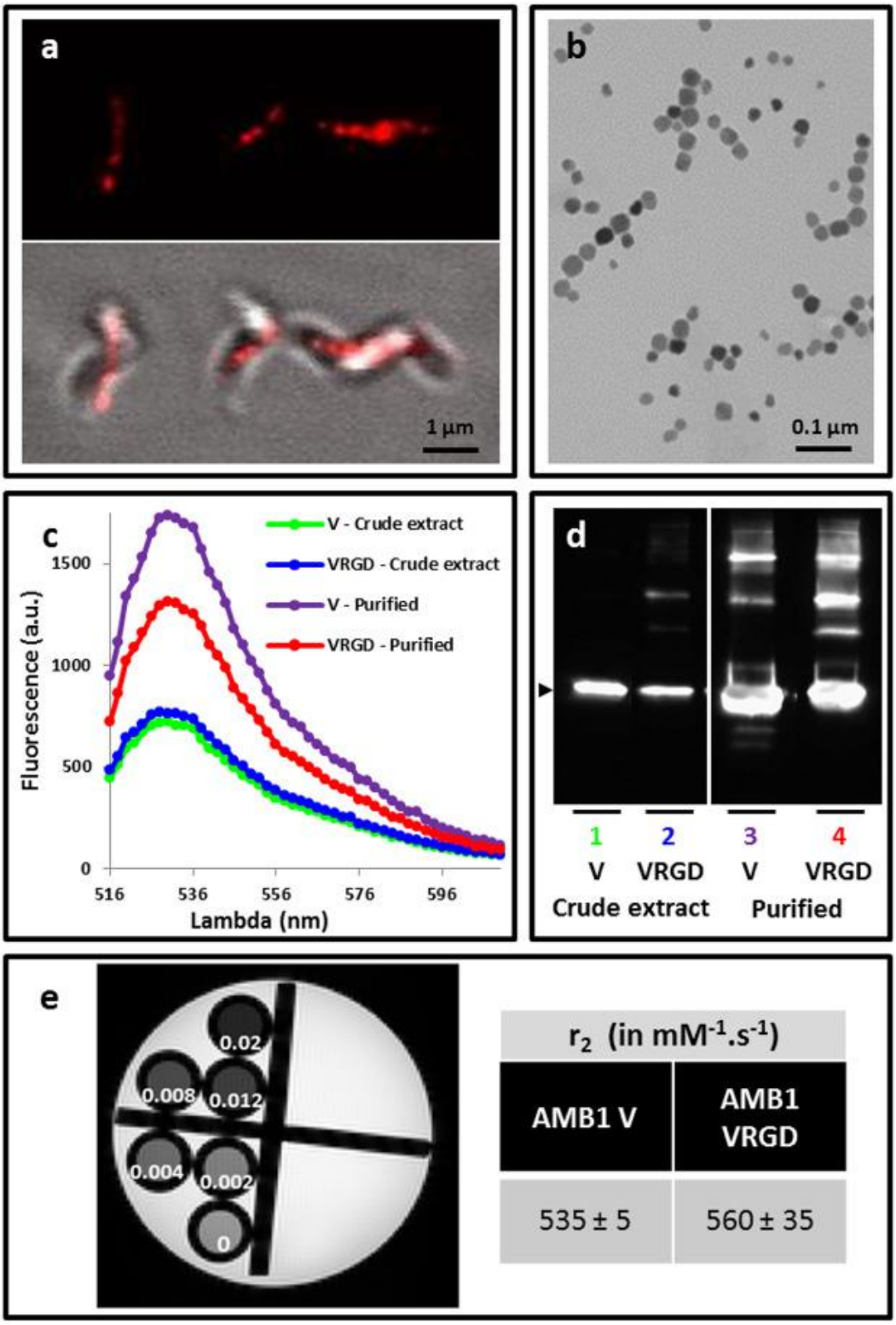

r_2 (in $mM^{-1}.s^{-1}$)	
AMB1 V	AMB1 VRGD
535 ± 5	560 ± 35

Fig. 1. **Production of functionalized magnetosomes**. *a/ Confocal microscopy images showing alive M. magneticum AMB-1 cells genetically modified to express the Venus-RGD protein at the magnetosome membrane. (Upper panel) Venus fluorescence (excitation at 514 nm). (Lower panel) Overlay of the bright-field and the Venus fluorescence images. b/ Representative TEM image of the magnetosomes suspension. c/ Fluorescence emission spectra (excitation at 490 nm) recorded on AMB-1 crude extracts after French press processing and on purified functionalized magnetosomes suspensions. d/ Western blotdetection of the MamC-Venus and MamC-Venus-RGD chimeric proteins (expected size 42 kDa, black arrow) with an anti-GFP antibody on AMB-1 cells crude extracts (1, AMB1 V; 2, AMB1 VRGD) and on purified functionalized magnetosomes suspensions (3, AMB1 V; 4,*

AMB1 VRGD). e/ T_2-weighted image revealing that MRI signal decreases when AMB1 VRGD magnetosomes concentration increases. The table shows the mean transverse relaxivity values measured in duplicates for AMB1 V and AMB1 VRGD suspensions.

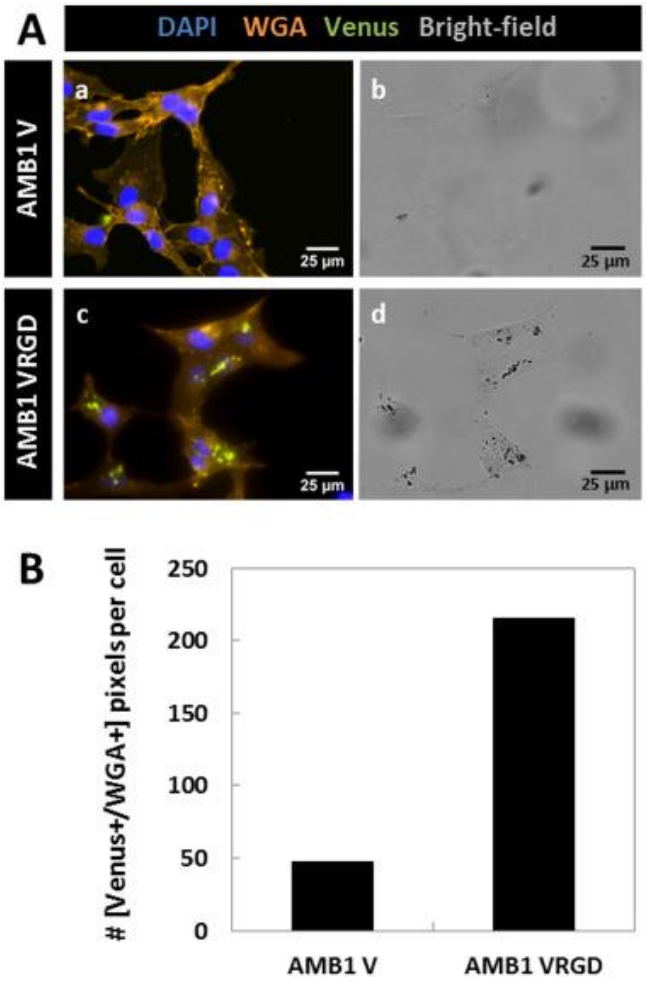

Fig. 2. ***In vitro* study of AMB1 VRGD affinity to U87 cells**. *A/ ×40 magnification fluorescence and bright-field images of U87 cells, after 3h30 of incubation with AMB1 V (control) or AMB1 VRGD (2 mg_{Fe}/L). A-a,c/ Merged fluorescence images show cell nuclei (DAPI staining in blue), cell membranes (Texas Red, Wheat Germ Agglutinin staining in orange), V or VRGD proteins (YFP in green). A-b,d/ Bright-field images show clusters of iron-oxide crystals. B/ Quantification of [Venus+/WGA+] pixels is performed on mosaic images, obtained after the same incubation protocol (see Supplementary Fig. S2). Count of [Venus+/WGA+] pixels is normalized by the number of detected cell nuclei, and plotted for AMB1 V and AMB1 VRGD incubation conditions.*

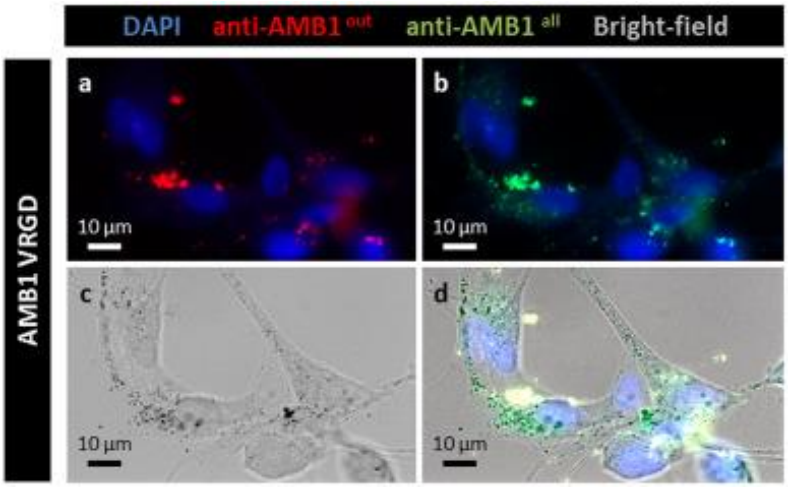

Fig. 3. ***In vitro*** **study of AMB1 VRGD internalization inside U87 cells.** *×63 magnification fluorescence and bright-field images of U87 cells, after 24 h of incubation with AMB1 VRGD (250 µg$_{Fe}$/L). a/ Merged fluorescence image acquired before detergent treatment shows cell nuclei (DAPI staining in blue) and magnetosomes localized only outside cells (anti-AMB1 staining revealed in red). b/ Merged fluorescence image acquired after detergent treatment shows cell nuclei (DAPI staining in blue) and all magnetosomes (anti-AMB1 staining revealed in green). c/ Bright-field image acquired after detergent treatment shows clusters of iron-oxide crystals. d/ Overlay of previous fluorescence and bright-field images (a,b,c) reveals in green magnetosomes localized only inside cells.*

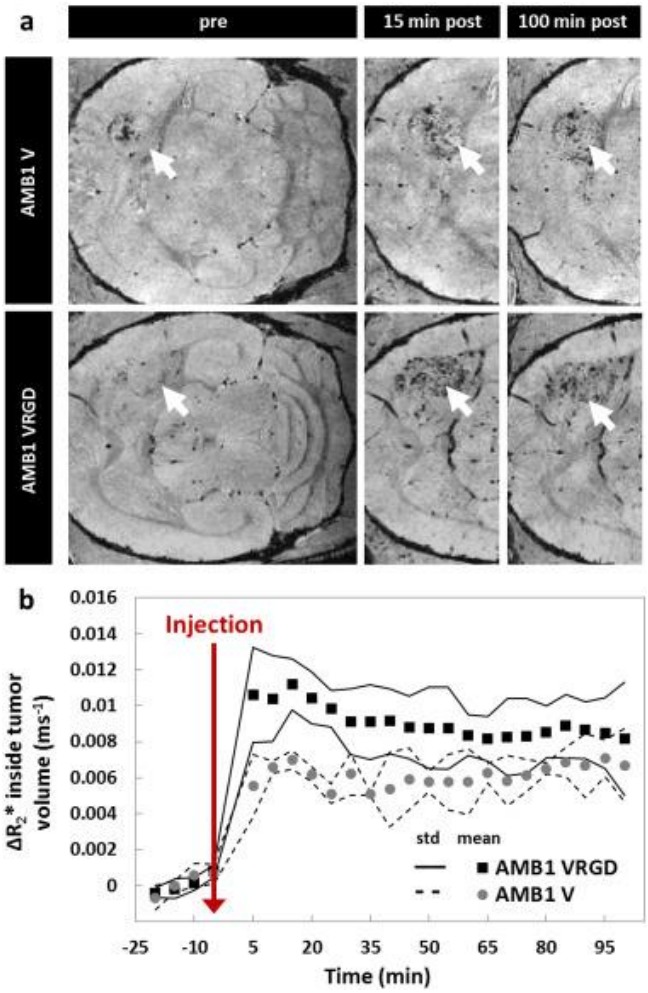

Fig. 4. **Short-term follow-up of MRI contrast in brain of glioblastoma-bearing mice after injection of functionalized (n = 4) and control (n = 2) magnetosomes**. *a/ FLASH images showing tumor area (white arrows), acquired before, 15 min and 100 min after magnetosomes injection. b/ Mean ΔR_2* values computed in tumor volume along time for each group of mice (black squares for AMB1 VRGD and gray circles for AMB1 V), with the corresponding standard deviations (solid lines for AMB1 VRGD and dashed lines for AMB1 V).*

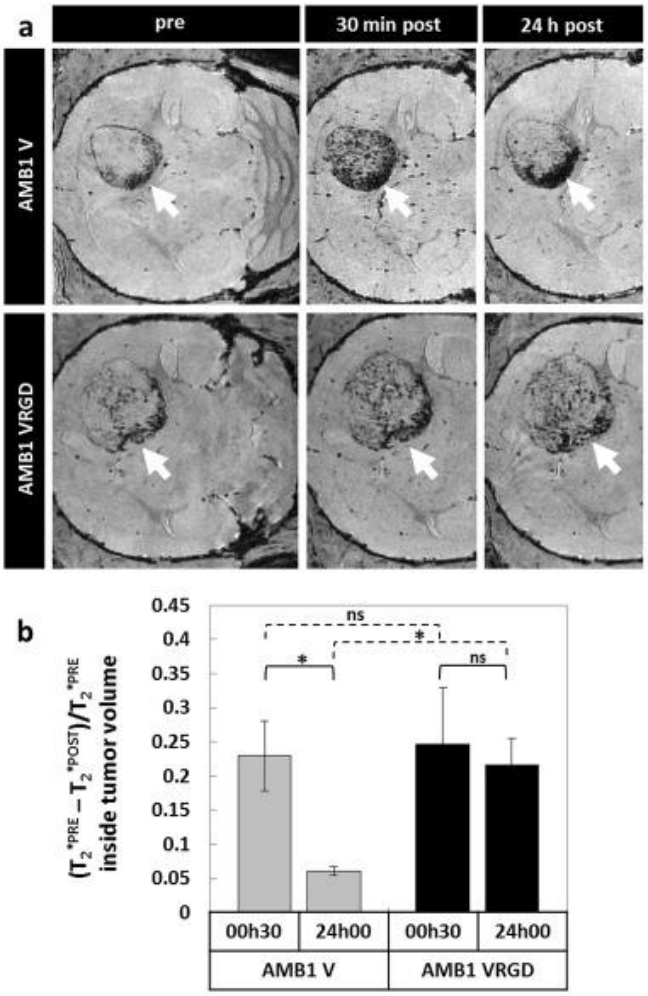

Fig. 5. ***Long-term follow-up of MRI contrast in brain of glioblastoma-bearing mice after injection of functionalized (n = 5) and control (n = 4) magnetosomes****. a/ FLASH images showing tumor area (white arrows), acquired before, 30 min and 24 h after magnetosomes injection. b/ Decrease of mean T_2* values, relative to pre-injection T_2^{*PRE} values, computed in tumor volume at 30 min and 24 h after magnetosomes injection (T_2* parametric maps presented in Supplementary Fig. S4). The statistical significance of differences, defined as p-value < 0.05 for a Wilcoxon test, is mentioned with an asterisk.*

Confocal microscopy images presented in Fig. 6b were collected on a Zeiss LSM780 confocal microscope (Carl Zeiss) using a Plan-Apochromat 63x/1.40 Oil DIC M27 objective. Alexa Fluor® 647 (revealing the anti-AMB1 antibody) was excited with an orange HeNe laser (633 nm), and emitted light was recorded between 567 and 627 nm. Alexa Fluor® 488 (revealing the anti-CD31 antibody) was excited with a blue argon ion laser (488 nm), and emitted light was recorded between 567 and 627 nm. Images were processed using Zen 2 software.

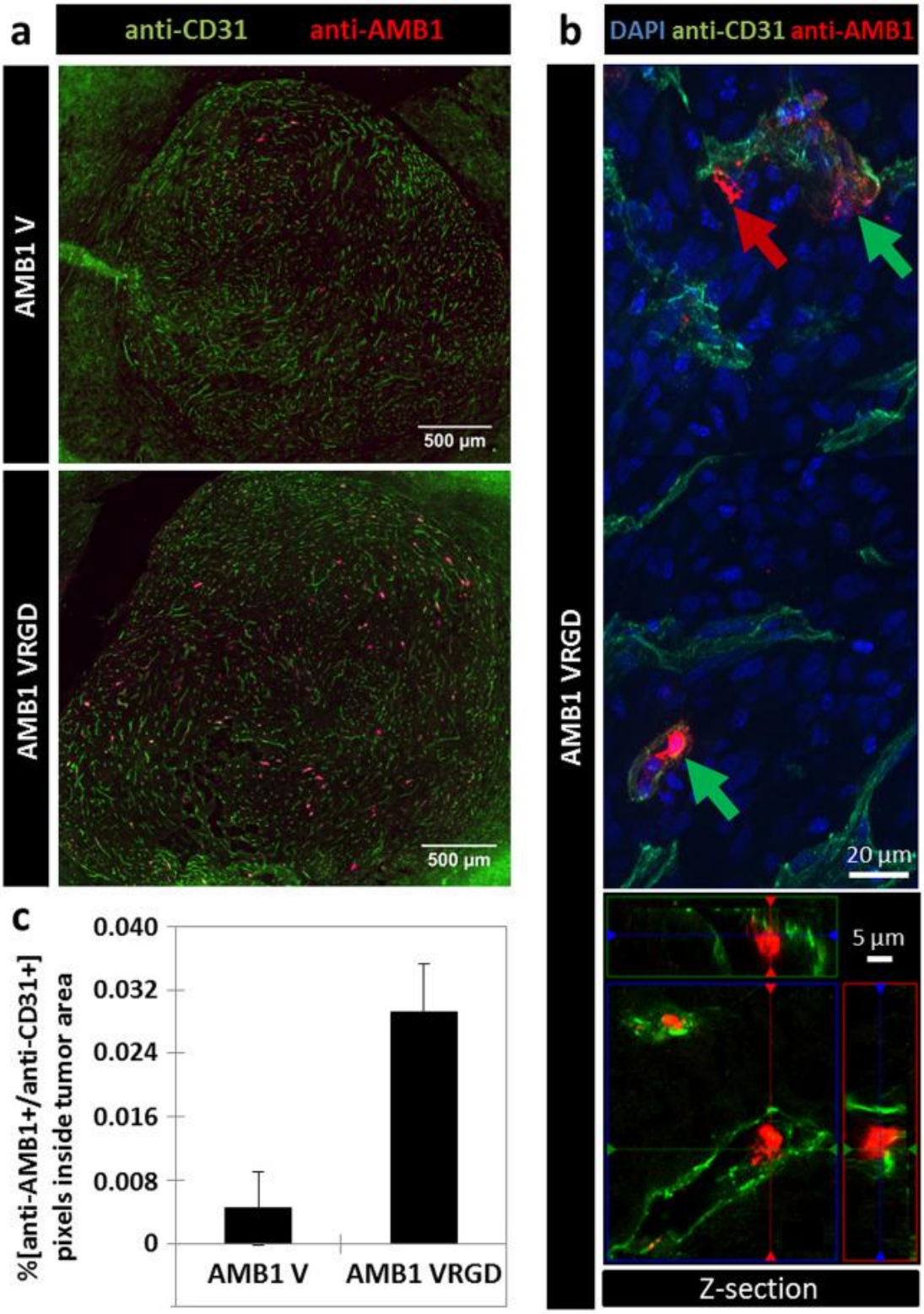

Fig. 6. ***Post mortem*** **evaluation of magnetosomes accumulation inside tumor**. *a/ ×20 magnification mosaic fluorescence images acquired after immunostainings of histological mouse brain slices (20 µm thickness), showing vessels (anti-CD31 staining revealed in green) and magnetosomes (anti-AMB1 staining revealed in red). Mice were injected with AMB1 V (upper panel) or AMB1 VRGD (lower panel) magnetosomes. b/ Upper panel: ×63 fluorescence image of an AMB1 VRGD-injected mouse brain slice showing magnetosomes within (green arrows) or outside (red arrow) vessels. DAPI-stained cell nuclei appear in blue. Lower panel: ×63 confocal Z-section (0.38 µm) with orthogonal views of the same mouse brain slice, confirming the co-localization of AMB1 VRGD magnetosomes (revealed in red)*

within vessels (revealed in green). c/ Quantification of anti-AMB1 positive pixels (magnetosomes) co-localized with anti-CD31 positive pixels (vessels) inside brain tumors (n = 3 mice analyzed for AMB1 VRGD group and n = 2 mice analyzed for AMV1 V group).

2.6. *Production of rabbit polyclonal antibodies against AMB1 magnetosomes*

450 µg (215 µL) of magnetosomes (AMB-1) were mixed with an equal volume of complete Freund's adjuvant (Sigma Aldrich) and were then injected subcutaneously into two 3 month-old New Zealand White rabbits (Charles River). The rabbits were fed *ad libitum* with a regular commercial diet (Kliba Nafag). The following injections were performed on days 28, 58 and 91 with incomplete Freund's adjuvant. 14 days after each boost, blood samples were collected from the rabbits and the antibodies against magnetosomes were titrated by ELISA test.

2.7. *In vitro U87 cells culture*

U87 cell lines from ATCC©, issued from human primary glioblastoma, were cultured in DMEM (Dulbecco's Modified Eagle's Medium) without phenol red (Sigma-Aldrich), with 10% of fetal bovine serum (Eurobio), 1% of glutamine (Lonza), 1% of pyruvate(Lonza), 1% penicillin/streptomycin (Lonza), and 7 µL/100 mL of gentamicin(Lonza). U87 cells were grown at 37 °C in a humidified atmosphere of 5% CO_2 for 3 days after seeding in glass bottom plates. Incubation with AMB1 V or AMB1 VRGD magnetosomes solution at 36 $\mu M_{[Fe]}$ was performed during 3h30 at 37 °C. 30 min before the end of incubation time, Wheat Germ Agglutinin (WGA, Eurobio) was added to the culture medium to reveal cells membrane. After 3h30 of incubation, glass plates were washed twice with PBS and mounted with Prolong® Gold Antifade Mountant with DAPI (4′,6-diamidino-2-phenylindole, ThermoFisher). Fluorescence microscopy images were acquired with an Axio Vision Observer microscope (Carl Zeiss) at ×20 magnification for mosaic images containing hundreds of cells, and at ×40 magnification for single field-of-view containing tens of cells. Cell nuclei were revealed in blue with DAPI, cell membranes in orange with WGA (Texas Red), V or VRGD proteins in green (YFP) and clusters of iron-oxide nanocrystals with dark spots in bright-field acquisitions. A second protocol was designed to distinguish magnetosomes localized inside and outside U87 cells. After 24 h incubation of U87 cells plates with AMB1 V or AMB1 VRGD (4.5 $\mu M_{[Fe]}$), cells were fixed with Paraformaldehyde (PFA) 4% during 10 min, and magnetosomes localized only outside cells were stained with a rabbit anti-AMB1 antibody specifically produced for this study (1/5000 dilution, 1 h incubation), revealed in red with a donkey anti-rabbit Alexa Fluor® 647 (Abcam). In a second step, U87 cells were permeabilized (30 min incubation in 0.2% Triton™ X-100 bath, Sigma-Aldrich), and all magnetosomes were stained with the same rabbit anti-AMB1 antibody (1/5000 dilution, 1 h incubation), revealed in green with a donkey anti-rabbit DyLight® 488 (Abcam). Then, $\alpha_v\beta_3$ integrins were stained with a mouse anti-$\alpha_v\beta_3$ antibody revealed in orange (MAB1976H-PE, Millipore, 1/100 dilution, 1 h incubation), and cell nuclei were revealed in blue with DAPI.

2.8. *In vitro measurement of magnetosomes transverse relaxivity r_2*

Transverse relaxivity r_2 was measured twice for each type of magnetosomes, AMB1 V and AMB1 VRGD. One measurement consisted in building a phantom containing 6 tubes filled with magnetosomes at different iron concentrations suspended in 0.3% w/w agar. T_2 parametric map of each phantom was acquired with an 11.7 T MRI BioSpec preclinical scanner (Bruker), using the following MSME (Multi-Slice Multi-Echo) sequence: 64 echoes spaced by 8 ms between 8 and 512 ms, TR = 5000 ms, in-plane field-of-view = 3 × 3 cm^2, in-plane spatial resolution = 250 × 250 μm^2, 6 slices of 1 mm thickness, 2 averages, total acquisition time = 20 min. After images reconstruction from MRI raw data using homemade Matlab routines (MathWorks), T_2 parametric maps were computed by fitting the signal intensity versus echo time using Bloch equations. Then, the mean proton relaxation rate R_2, equal to the inverse of transverse relaxation time T_2, was computed for each tube, and a linear fit of R_2 values versus iron concentrations was performed to estimate the transverse relaxivity r_2 as the slope of the fitted curve. Finally, the two r_2 measurements were pooled to estimate both mean r_2 value and standard deviation for each type of magnetosomes.

2.9. *U87 mouse model of glioblastoma*

All *in vivo* experiments were conducted in strict accordance with the recommendations of the European Community (2010/63/EU) and the French legislation (decree n°2013-118) for use and care of laboratory animals. The protocol for contrast agent injection has been approved by the Comité d'Éthique en Expérimentation Animale du Commissariat à l'Énergie Atomique et aux Energies Alternatives – Direction des Sciences du Vivant Ile-de-France (CETEA/CEA/DSV IdF) under protocol ID 12-058. U87 cells were cultured and amplified using the protocol already described for *in vitro* studies. Brain tumors were induced by intracerebral injection of U87 cells (120 000 cells/2 µL) to athymic immunodeficient nude mice (NMRI-nu, Janvier). For the surgery, 6 weeks old mice were anesthetized with an intraperitoneal injection of Ketamine/Xylazine (100/10 mg/kg, 10 mL/kg) and maintained in a stereotaxic frame. A 1 mm hole was drilled in the skull 2 mm right to the bregma, and then U87 cells suspended in PBS were slowly injected with a Hamilton syringe at 3.5 mm depth. MRI experiments were launched around 21 days after implantation, when the tumor diameters were around 3 mm.

2.10. *In vivo MR-based molecular imaging studies*

For both short-term (0–100 min after injection) and long-term (0–24 h after injection) studies, MRI acquisitions were performed on an 11.7 T MRI BioSpec preclinical scanner equipped with a radiofrequency cryogenic coil dedicated to mouse brain (Bruker). Mice were anesthetized using an air/O_2 mixture (50:50) and isoflurane(3%), before being positioned into dedicated cradle. Respiration rate was continuously monitored and body temperature was kept close to 37 °C thanks to a warm water circulation system. After acquiring baseline scans, the cradle was removed out of the magnet tunnel while keeping the mouse positioned, and injection of 200 µmol of iron per kg of body weight of magnetosomes suspension

(54 $mM_{[Fe]}$) was performed at the mouse caudal vein with a 29 G syringe. The cradle was afterward quickly inserted back into the tunnel for acquiring post-injection MRI scans.

To reveal the T_2* negative contrast induced by the injection of magnetosomes, a T_2*-weighted FLASH (Fast Low Angle SHot) sequence was used with the following parameters: TE/TR = 8/1600 ms, in-plane field-of-view = 1.92 × 1.47 cm^2, in-plane spatial resolution = 75 × 75 μm^2, 90 slices of 75 μm thickness, 1 average, total acquisition time = 5 min. To obtain more quantitative data on magnetosomes biodistribution, a MGE (Multi Gradient Echo) sequence was acquired with the following parameters: TE = 3.5/7/10.5/14/17.5/21/24.5/28 ms, TR = 90 ms, field-of-view = 1.90 × 1.42 × 0.80 cm^3, spatial resolution = 100 × 100 × 100 μm^3, 1 average, total acquisition time = 17 min. After images reconstruction, T_2* parametric maps were computed by fitting the signal intensity versus echo time using Bloch equations.

For the short-term study, mice were divided in two groups: n = 4 received AMB1 VRGD injection and n = 2 received AMB1 V injection. For each mouse, the MRI experiment started by acquiring a baseline of 4 FLASH images, then injecting magnetosomes and consecutively acquiring 20 FLASH images to dynamically follow the MRI contrast enhancement in the tumor briefly after injection. For the long-term study, mice were also divided in two groups: n = 5 received AMB1 VRGD injection and n = 4 received AMB1 V injection. For each mouse, the MRI experiment started by acquiring one FLASH image and one MGE image as baseline, injecting magnetosomes and then acquiring one MGE image followed by one FLASH image 30 min post-injection. The animal was removed from the cradle and woke up after the last scan. 24 h after magnetosomes injection, another MGE image followed by a FLASH image were acquired.

Right after the last MRI session, mice were euthanized with an overdose of Xylazine/Ketamine, intracardiacally perfused with NaCl 0.9% to remove blood and then fixed with PFA 4%. Brains were extracted, post-fixed 2 h in PFA 4%, soaked in sucrose solutions (15% followed by 30%), frozen by immersion in −30 °C isopentane to be finally stored at −80 °C for histological analysis.

2.11. *In vivo MR images processing*

All *in vivo* MRI data were processed with homemade Matlab routines. For the short-term study, brain tumor volumes were manually segmented on reconstructed FLASH images. To follow the contrast enhancement in the tumor area, the normalized R_2* (= $1/T_2$*) enhancement was estimated as follows [34]: $\Delta R2*t=1TElogmeanStPRESt$, S being the FLASH signal inside the tumor. This ΔR_{2^*} parameter was computed for the different time points *t* after magnetosomes injection, and the mean and standard deviation of ΔR_{2^*} for both groups of mice were plotted versus time (Fig. 4b).

For the long-term study, brain tumor volumes were manually segmented on T_{2^*}parametric maps reconstructed from MGE images. To follow the contrast enhancement in the tumor area, the normalized decrease of T_{2^*} was estimated for the different time points *t* after

magnetosomes injection as follows: $\Delta T2*(t)=(T2*PRE-T2*POST(t)T2*PRE)$. To compare the tumor targeting properties of injected magnetosomes, the means of ΔT^*_2 estimated for all tumor voxels were pooled together for both groups of mice at 30 min and 24 h post-injection (Fig. 5b). A non-parametric Wilcoxon signed-rank test was ran to evaluate the statistical significance of the 30 min versus 24 h post-injection differences, as well as the AMB1 V versus AMB1 VRGD differences.

2.12. *Post mortem histological analysis*

Brain samples were cut into 20 µm thickness slices with a cryomicrotome, and positioned on glass slides. Immunohistochemical stainings were performed to stain *i)* vessels with a rat anti-CD31 antibody (MCA2388, AbD Serotec, 1/50 dilution, 1 h incubation) revealed in green with a donkey anti-rat Alexa Fluor® 488 (Abcam), *ii)* $\alpha_v\beta_3$ integrins with a mouse anti-$\alpha_v\beta_3$ antibody revealed in orange (MAB1976H-PE, Millipore, 1/100 dilution, 1 h incubation), and *iii)* AMB1 magnetosomes with the rabbit anti-AMB1 antibody specifically produced for this study (1/5000 dilution, 1 h incubation), revealed in red with a donkey anti-rabbit Alexa Fluor® 647 (Abcam). Finally stained histological slices were mounted with Prolong® Gold Antifade Mountant with DAPI (ThermoFisher) to reveal cell nuclei in blue. Fluorescence microscopy images were acquired with an Axio Vision Observer microscope (Carl Zeiss) at ×20 magnification for mosaic images covering the whole tumor area, and at ×63 magnification for single field-of-view focusing on structures of interest inside the tumor.

2.13. *Fluorescence images processing*

All fluorescence microscopy data were processed using homemade Matlab routines. After four times downsampling of native images, quantification of *in vitro*data (Fig. 2B) was done by thresholding orange (WGA, cells membrane) and green (Venus, magnetosomes) channels. The image of thresholded orange channel was slightly dilated to smooth borders and fill potential holes. Both masked images were then clusterized: if a green cluster overlapped an orange one, it was considered as co-localized (Venus+/WGA+), otherwise it was considered as isolated (Venus+/WGA-).

A similar procedure was applied to analyze *post mortem* histological data on whole tumor (Fig. 6c). One coronal slice containing a full section of the tumor and crossing its center was analyzed per mice (n = 3 animals in AMB1 VRGD group and n = 2 in AMB1 V group). After a manual segmentation of the tumor zone on the orange channel ($\alpha_v\beta_3$ integrins), the green (anti-CD31, vessels) and red (anti-AMB1, magnetosomes) channels were thresholded. The image of thresholded green channel was slightly dilated, and then both masked images were clusterized: a red cluster detected in the tumor was considered inside a vessel when an overlap with a green cluster occurred (anti-AMB1+/anti-CD31+).

3. Results

We established in a previous study the suitability of wild-type magnetosomes to be used as highly efficient T_2-shortening agents for *in vivo* brain imaging in mice with MRI [17]. The

following Results section describes the preparation of RGD-functionalized magnetosomes suspensions readily injectable into the mouse blood circulation, the assessment of the targeting strategy on U87 tumor cell cultures and finally its validation *in vivo* on glioblastoma-bearing mice assisted by high-field 11.7 T MRI.

3.1. *Injectable suspensions of genetically modified magnetosomes*

The magnetotactic *M. magneticum* AMB-1 strain was genetically modified to express at the magnetosome surface a RGD peptide (known to target $\alpha_v\beta_3$ integrin receptors) attached to the Venus variant of the Green Fluorescent Protein (GFP). To do so, we designed a transcriptional fusion between the DNA sequences encoding Venus (AMB1 V strain) or Venus-RGD proteins (AMB1 VRGD strain) with the *mamC*gene coding for an abundant protein of the magnetosome membrane. The Venus protein served as a fluorescent marker during the magnetosomes purification, as a spacer for an efficient display of the RGD peptide at the magnetosome surface and as a fluorescent reporter for fluorescence microscopy. In live bacteria, one could observe in confocal microscopy a series of Venus fluorescence foci aligned within the cell, reminiscent of the magnetosomes chain organization (Fig. 1a), hinting at a proper functionalization of the magnetosome membranes with the Venus and Venus-RGD proteins. Magnetosomes were then magnetically extracted from crude cellular lysates after mechanical disruption by a French press, and after several washing steps, the purified magnetosomes were conditioned in readily injectable doses at the final iron concentration of 54 mM. The nanoparticle size distribution was computed from TEM images (Fig. 1b), resulting in a mean typical length value of 45 nm, and the persistence of the functionalization was verified throughout the production process with fluorescence spectroscopy and Western blot analysis(Fig. 1c and d), which confirmed the presence of a functional Venus protein (hence the RGD peptide for AMB1 VRGD) in the final injectable suspensions. Magnetosomes were thus successfully genetically functionalized and prepared into injectable suspensions.

Functionalized magnetosomes were intended for MRI studies as T_2-shortening agents, we then demonstrated *in vitro* that their contrasting properties were not altered by the genetic functionalization. A decrease of T_2-weighted MRI signal was observed when magnetosomes concentration increased, demonstrating the negative contrast induced by magnetosome iron-oxide core (Fig. 1e). Transverse relaxivities r_2 were estimated as the slope of R_2 (= $1/T_2$) values versus iron concentrations (Supplementary Fig. S1): r_2 values of 535 $mM^{-1}s^{-1}$ and 560 $mM^{-1}s^{-1}$ were found for AMB1 V and AMB1 VRGD magnetosomes respectively, in line with our previous study with wild-type AMB-1 magnetosomes [17].

3.2. *Specific binding of RGD magnetosomes to U87 tumor cells*

As a prerequisite to the injection to alive glioblastoma-bearing mice, we assessed the affinity of the RGD magnetosomes for U87 cells issued from human primary glioblastoma, known to overexpress $\alpha_v\beta_3$ integrins [35,36]. Thanks to the Venus fluorophore decorating the membrane surface for both control (AMB1 V) and RGD (AMB1 VRGD) magnetosomes, the

fate of these nanoparticles could be easily followed by fluorescence microscopy. U87 cells were incubated during 3h30 with the magnetosomes at a final iron concentration of 36 µM. Cell membranes and nuclei were then stained respectively with Wheat Germ Agglutinin (WGA) and DAPI, before cells observation by fluorescence and in bright-field microscopy. In the representative fluorescence images shown in Fig. 2A, magnetosomes (Venus fluorescence) appear in green, cell membranes in orange and nuclei in blue, whereas iron-oxide cores are revealed as dark spots in bright-field images. Many bright Venus spots seemed mostly co-localized with U87 cells when they were previously incubated with AMB1 VRGD magnetosomes (Fig. 2A, panel c), while very few Venus fluorescence foci could be seen with the control AMB1 V magnetosomes (Fig. 2A, panel a). In both cases, Venus fluorescence overlapped with the iron-oxide core observed in bright-field images (Fig. 2A, panels b and d). From these observations, we can conclude that after 3h30 incubation with U87 cells, Venus fluorescence at the magnetosome membranes is still observed, and magnetosomes mostly interact with U87 cells when they are functionalized with the RGD peptide.

We quantified the fraction of magnetosomes bound to or internalized into U87 cells with both RGD-functionalized and control magnetosomes, by acquiring in each condition mosaic images at ×20 magnification containing hundreds of cells (Supplementary Fig. S2), and by computing the ratio between Venus pixels (magnetosome) overlapping with WGA pixels (cell membrane), normalized by the number of cells in the image (corresponding to the number of DAPI-stained nuclei). About 92% of the detected Venus fluorescence overlapped with U87 cells for both control and RGD magnetosomes, the remaining fraction likely resulting from residual magnetosomes having escaped the washing steps and bound to the glass plate. From the histogram shown in Fig. 2B, we could estimate a 4.5 increase of cell-bound fluorescence – hence magnetosomes – with AMB1 VRGD treatment compared with AMB1 V one. We demonstrate here the efficacy of our targeting strategy with RGD-functionalized magnetosomes on U87 tumor cells with a simple and rapid fluorescence-imaging assay.

3.3. *RGD magnetosomes internalization into U87 cells*

Active internalization of RGD-functionalized nanoparticles upon binding thanks to integrin recycling [37,38] is known to efficiently load the targeted cells with nanoparticles. We thus investigated whether magnetosomes can be internalized after binding to U87 cells thanks to RGD peptide. The apparent co-localization observed in the fluorescence images between cell membranes and magnetosomes (Fig. 2) could result either from nanoparticles bound at the cell surface or internalized into the cells. Since we could not distinguish between the two situations with Venus fluorescence alone, we used a polyclonal antibody raised against the magnetosome membrane to discriminate magnetosomes sitting outside from those sitting inside U87 cells. Furthermore, the incubation time was lengthened up to 24 h to insure enough internalization if any, and the magnetosomes dose was diminished to 4.5 µM to avoid fluorescence saturation. Briefly, after 24 h of incubation of either the control (AMB1

V, Supplementary Fig. S3) or RGD-functionalized (AMB1 VRGD, Fig. 3) magnetosomes with intact U87 cells, followed by washes and cell fixation, magnetosomes bound at the outer surface of the U87 cells were revealed by immunohistochemical staining (anti-AMB1^{out}, red channel in Fig. 3a). Cells membranes were subsequently permeabilized by a mild detergent treatment allowing the antibodies to diffuse into the cytosol, thus resulting in the immunohistochemical detection of the entire magnetosomes population, *i.e.* those bound at the surface and those internalized (anti-AMB1^{all}, green channel in Fig. 3b). The internalized fraction was simply deduced by signal difference obtained before and after detergent treatment, and appeared in green when channels were merged while the outside bounded fraction appeared in yellow (Fig. 3d). For the unlabeled magnetosomes, we observed that the permeabilization of the plasma membranes did not bring out any more fluorescence but the yellow one (Supplementary Fig. S3), meaning that the entire fluorescence sits outside of the cells, because of unspecific attachment to U87 cells or to the bottom of glass plates. This was not the case with the RGD magnetosomes, where the permeabilization of the plasma membranes enabled the detection of many discrete green fluorescent dots situated within the cell boundaries in addition to the yellow ones (Fig. 3d).

The results presented in Fig. 3 suggest an active transport of the RGD magnetosomes across the cell membrane upon binding to the $\alpha_v\beta_3$ integrins, which is in accordance with observations previously made for other, non-biogenic, RGD-functionalized nanoparticles [31]. Together, these *in cellulo* data indicate that the RGD-functionalized magnetosomes target the $\alpha_v\beta_3$ integrin receptorsoverexpressed by U87 cells issued from human primary glioblastoma and accumulate within the cytosol, therefore justifying further *in vivo* investigations in glioblastoma-bearing mice with high-field MRI.

3.4. In vivo demonstration of RGD magnetosomes affinity and retention in brain tumor

Firstly, *in vivo* MRI experiments were performed by injecting magnetosomes (control or RGD) to a mouse model of glioblastoma, in order to validate that both magnetosomes could equally circulate in blood stream for a couple of hours, especially in the brain and in the tumor. AMB1 V can be used as a control for AMB1 VRGD in *in vivo* studies only if they produce similar MRI contrast, meaning that a comparable amount of magnetosomes reaches tumor vessels. This has been tackled by following the contrast in the mouse brain with the highest imaging rate and as long as possible right after magnetosomes intravenous injection. This protocol was designed to follow during 100 min the MRI contrast enhancementinduced in brain tumor after RGD-functionalized or control magnetosomes injection to tail vein of glioblastoma-bearing mice. A T_2*-weighted FLASH imaging strategy has been chosen to ensure an imaging rate of one image every 5 min, still providing very high spatial resolution (75 µm isotropic). FLASH images acquired before and 15 min after injection revealed that both types of magnetosomes injections led to a very rapid and abundant increase of the number of detected hypo-intense voxels in the tumor area (white arrows in Fig. 4a). Furthermore, this increase of hypo-intense voxels number seemed to maintain in time until 100 min. Observation of FLASH images was assessed with a semi-quantitative measurements of MRI signal loss (ΔR_{2^*} parameter), by

normalizing the signal in the tumor by its value before injection. ΔR_{2^*} values showed a sharp increase right after injection and then reached a similar plateau in each group of mice (control and RGD-functionalized magnetosomes, grey circles and black squares in Fig. 4b respectively), revealing that in the time frame of 100 min, both injected magnetosomes steadily circulated in tumor vasculature.

These observations settle *in vivo* the high MRI contrasting properties of the magnetosomes suspensions prepared for this study, in line with the *in vitro*demonstration by the transverse relaxivity measurements (Fig. 1e). Magnetosomes steadily circulating in *in vivo* physiological condition during at least 100 min means that their blood half-lives are longer than 2 h. Thus, both magnetosomes present good bio-compatibility properties and similar *in vivo* contrasting properties, which validates the use of AMB1 V as a control for AMB1 VRGD for the *in vivo* study of magnetosomes binding. Furthermore, it assesses that AMB1 magnetosomes, unlabeled or functionalized, present similar *in vivo* behaviors: they both enhance efficiently tumor vasculature until 2 h post-injection, and can be used as efficient contrast agent for brain tumor imaging.

Secondly, we investigated if magnetosomes binding was occurring at tumor area by measuring magnetosomes load inside tumor volume 24 h after their intravenous injection, following a complete washout of the magnetosomes from the blood stream. The molecular imaging protocol was designed to provide a quantitative measure of magnetosomes uptake by the mouse brain tumor from 30 min to 24 h post-injection, and to investigate whether the RGD functionalization increases this magnetosomes uptake. The literature indicates that blood half-lives of iron-oxide nanoparticles in tumor vessels generally lie in the hour range, and then nanoparticles are mostly found in macrophages 24 h post-injection [3]. Thus chemically-synthetized iron-oxide nanoparticles are cleared from blood stream after 24 h, so we chose to investigate magnetosomes retention in the mouse brain tumor 24 h after injection. In addition to FLASH images that were useful for magnetosomes visualization, the molecular imaging protocol included the acquisition of a parametric MGE sequence, in order to quantitatively compare scans when the animal was removed from the scanner between two imaging sessions (between 0/30 min and 24 h). This study confirmed the previous results obtained during the 100 min post-injection follow-up: numerous hypo-intense voxels were observed inside the tumor area on FLASH images for both groups of mice at 30 min post-injection (white arrows, 30 min post-injection images, Fig. 5a). After 24 h, dark areas inside the tumor on FLASH images seemed to maintain in AMB1 VRGD condition, while the MRI signal has increased in AMB1 V condition (comparison between 30 min and 24 h post-injection images, Fig. 5a). However, a quantitative parameter was required to compare groups of mice together: T_2* parametric maps (Supplementary Fig. S4) were acquired to compute ΔT^*_2 values, which represent the loss of MRI signal in the tumor post-injection, relative to the signal in the tumor before injection. Thus ΔT^*_2 values were used as indirect measures of magnetosomes uptake by mouse brain tumor (Fig. 5b). A high and similar uptake was observed in both groups 30 min after injection, which is in agreement with the

previous experiment and corroborates that both magnetosomes are comparable blood pool agents, *i.e.* the RGD functionalization does not alter their blood circulation properties. Nevertheless, a significant difference in uptake between the two treatments was observed 24 h post-injection, in favor of AMB1 VRGD. No significant difference of magnetosomes uptake inside the tumor was observed between 30 min and 24 h post-injection acquisitions in AMB1 VRGD group, meaning that magnetosomes seemed to stay inside tumor area when functionalized. However, a significant tumor clearance occurred after 24 h in AMB1 V group. In addition to the passive accumulation of magnetosomes inside the tumor (illustrated in Fig. 5b by the AMB1 V uptake remaining 24 h post-injection), our results clearly establishes that the RGD functionalization enhances brain tumor targeting properties of magnetosomes, leading to a high and constant level of tumor iron uptake during at least 24 h.

Thirdly, the specific accumulation of RGD magnetosomes inside brain tumor, observed *in vivo* 24 h after injection, was assessed by *post mortem* histological data acquisitions. A specific immunohistochemical staining was performed on mouse brain slices to reveal magnetosomes localization inside tumor volume, using the dedicated polyclonal antibody directed against AMB1 magnetosomes. Mosaic fluorescence images of brain tumor showed tumor vessels (revealed with anti-CD31 staining) overlapping with magnetosomes signal for both AMB1 V and AMB1 VRGD conditions (Fig. 6a). AMB1 signal was found more abundant in AMB1 VRGD treated mouse compared to AMB1 V one, establishing that the RGD functionalization increases magnetosomes retention inside brain tumor. ×63 magnification fluorescence images focusing on tumor area of mice treated with AMB1 VRGD confirmed that the red fluorescence signal associated with magnetosomes (anti-AMB1 staining) could be mostly found overlapping with the green fluorescence signal of blood vessels (anti-CD31 staining), as illustrated by green arrows on Fig. 6b (upper panel). Besides, few magnetosomes seemed to be localized outside vessels, as illustrated by the red arrow on Fig. 6b (upper panel). Images obtained with confocal microscopy confirmed the localization of RGD-functionalized magnetosomes within tumor vessels, as expected for a circulating blood contrast agent (Fig. 6b, lower panel). A quantification step was applied on mosaic fluorescence images (see Supplementary Fig. S5) acquired for n = 2 mice treated with AMB1 V and n = 3 mice treated with AMB1 VRGD, to measure the percentage of pixels in the tumor that were positive to AMB1 red fluorescence signal and overlapped with vessels green fluorescence signal. This quantitative measure revealed that tumors treated with AMB VRGD presented 6.5 times more [anti-AMB1+/anti-CD31+] pixels compared to the ones treated with AMB1 V, which cross-validated the increased uptake observed with *in vivo* MRI measurements. In each condition, around 10% of the AMB1 red fluorescence signal were not localized within vessels, which might be explained by nonspecific uptake, from macrophages for example, or by EPR effect. Thus, this *post mortem* histological analysis confirms *in vivo* MRI results, by demonstrating a higher uptake of magnetosomes by brain tumor for mice treated with AMB1 VRGD.

4. Discussion

We successfully designed and produced genetically modified magnetosomes from wild-type AMB1 strain of magnetotactic bacteria, integrating a RGD peptide in order to target $\alpha_v\beta_3$ integrin receptors, combined with a fluorescent protein marker (Venus) successfully used to follow the particles in *in vitro* studies. We evidenced that the MRI contrasting properties at 11.7 T measured for unlabeled and functionalized magnetosomes (r_2 values around 550 $mM^{-1}s^{-1}$) are comparable and in good agreement with previous measurements obtained for other magnetotactic bacteria strains and at different intensities of magnetic field [17,20,22]. These high r_2 values compared to those of many chemical nanoparticles [3] lead to high MRI sensitivity, which makes magnetosomes very good candidates for MR-based molecular imaging applications.

We demonstrated *in vitro* that RGD peptides, bioproduced at magnetosomes surface by magnetotactic bacteria, exhibit sufficient affinity to specifically bind to their target, the $\alpha_v\beta_3$ integrins overexpressed at U87 tumor cells membrane. We revealed that this effective binding can lead to magnetosomes internalization inside tumor cells, thanks to a specific experimental protocol set up to differentiate magnetosomes standing outside or inside U87 cell membrane. The results confirmed that the interactions between our functionalized probe and its target correspond to a highly dynamic process, from the binding up to the internalization [37]. Indeed, $\alpha_v\beta_3$ integrins are constantly recycled from cell membrane to intracellular vesicles, which are then recycled back to membrane with a half-life around 10 min [29]. Therefore, RGD-functionalized magnetosomes can bind to tumor cells membrane and afterward being internalized, which implies that one should take great care of both dosage and injection timing when optimizing the tumor targeting efficiency.

Molecular imaging of U87 brain tumor has been carried out *in vivo* on mice at two different time scales after magnetosomes injection. This enabled to tackle in a first step the general behavior of AMB1 magnetosomes *in vivo*, in order to assess that both AMB1 V and AMB1 VRGD are efficient MRI contrast agents and present comparable properties. Indeed, in the first hundred minutes post-injection, both probes show a high efficiency in enhancing MRI contrast between tumor and healthy brain, and a similar bio-availability in the tumor area. Time frame of imaging compared to administration strategy of molecular imaging probe is actually a key parameter. Non-functionalized iron-oxide nanoparticles are expected to be blood pool agents at the hour scale, and are afterward suitable for reticuloendothelial system (macrophages, liver, spleen, lymph node, among others) imaging since they are eliminated from the blood stream by this path [2,3]. Inside brain tumors, the increased permeabilization of blood-tumor barrier (EPR effect) allows a passive targeting of tumor parenchyma by nanoparticles [27]. This passive targeting through EPR effect is highlighted by the tumor area presenting darker signal than healthy brain until 100 min after magnetosomes injection. Furthermore, this passive targeting can also be appreciated as the remaining tumor uptake of AMB1 V magnetosomes 24 h post-injection. Regarding RGD-functionalized magnetosomes, their active targeting properties combined to the EPR effect lead to a significantly higher retention inside tumor parenchyma compared to control magnetosomes, as highlighted by

24 h post-injection results. This outcome is also strongly cross-validated by *post mortem* histological data that confirm a higher retention of magnetosomes in tumors of AMB1 VRGD treated mice compared to controls. The RGD peptide localized at magnetosome membrane can specifically target tumor biomarkers, such as $\alpha_v\beta_3$ integrins overexpressed by tumor neo-angiogenic vessels, leading AMB1 VRGD to be held into tumor area.

In these *in vitro* and *in vivo* studies, magnetosomes have been incubated with mammalian cells and injected to mice, and it is noteworthy that no specific adverse effect was observed (good cell viability, good general condition of animals after injection up to 24 h). Our observations were consistent with recent investigations on the biocompatibility of purified magnetosomes: several in-depth studies, performed on either rats or mice, showed no toxicity of the magnetosomes used at this range of low concentrations (200 µmol of iron per kg of body weight of magnetosomes suspension), and revealed that magnetosomes appeared to be fully degraded *in vivo* after 28 days by cell lysosomes [19,39–44]. Nevertheless, further biodistribution and toxicity studies need to be carried out to unravel the long term fate of our functionalized magnetosomes.

Our *in vivo* MRI results demonstrated the feasibility of using a fully biogenic molecular imaging probe to target brain tumor in a mouse model of human glioblastoma. Nevertheless, some issues regarding the optimization of both specificity and sensitivity of this targeting remain to tackle. Firstly, regarding the chosen application, the next step could be to study the influence of both dose and imaging timing on detection of iron accumulation inside the tumor. For example, it would be very interesting to investigate different injection procedures: in this study, we chosen a standard intravenous bolus injection, but trying continuous infusion of smaller magnetosomes doses on a longer time frame might increase the tumor uptake, since it is expected to maximize the probe exposure to its target. Moreover, to further enhance targeting properties of functionalized magnetosomes, replacing linear RGD peptide for a more affine form, like the cyclic penetrating RGD for example [28], could help to increase probe specificity. Finally, theranostic applications could be considered by setting new hyperthermia protocols. Hyperthermia is a well-known and extensively investigated technique for thermotherapy of tumors [7], and several studies have already demonstrated the therapeutic effect induced by magnetic hyperthermia applied to magnetosomes directly injected inside the tumor [45,46]. The efficiency of tumor treatment by hyperthermia could be improved thanks to the active targeting of neo-angiogenic vessels localized inside tumor obtained with functionalized magnetosomes. Furthermore, it also opens the way to less invasive magnetic hyperthermia protocols, by replacing intra-tumoral injection with intravenous one.

5. Conclusion

In summary, this work embodies the first achievement in producing, under biological processes, a specific and sensitive molecular imaging probe for MRI. Knowing that magnetosomes size and shape are strongly strain-dependent [12], it is then possible to

further tune MRI contrasting properties and tailor targeting affinity by changing bacteria strain and strategy for genetic modifications. Magnetotactic bacteria would therefore become integrated nano-factories providing customized functionalized contrast agents for a wide range of diagnostic and theranostic applications. This proof-of-concept not only paves the way for further improvements regarding our application, but also strengthens the potential interest of developing biogenic probes for *in vivo* molecular imaging applications.

Author contributions

S.P., G.A.-P., M.P., C.T.L., D.P. and N.G. planned and performed experiments regarding magnetosomes production and characterization.

M.B. and F.G. planned and performed *in vitro* experiments with U87 cells.

M.B., F.G., E.S. and S.M. planned and performed *in vivo* MRI experiments with U87 mouse model of glioblastoma.

M.B., F.G. and S.P. planned and performed *post mortem* histological analyses.

L.B. planned and performed experiments to produce specific antibody raised against magnetosomes membrane.

L.B., D.P., N.G. and S.M. managed the study and provided its funding as part of the MEFISTO project.

All authors contributed to manuscript edition.

Acknowledgments

This work is part of the MEFISTO project, supported by the French public funding agency ANR (Agence Nationale pour la Recherche, APP-P2N 2012). France Life Imaging is acknowledged for funding the 11.7 T preclinical MRI scanner of NeuroSpin. The authors also thank the Institut de Radioprotection et de Sûreté Nucléaire of Cadarache for access to their electron microscopy facility. Support for the Zeiss LSM780 microscopy equipment is provided by the Région Provence Alpes Côte d'Azur, the Conseil Général des Bouches du Rhône, the Ministère de la Recherche, the Centre National de la Recherche Scientifique and the Commissariat à l'Énergie Atomique et aux Énergies Alternatives. Noël Converset (Zeiss, France) is gratefully acknowledged for his help to acquire data with the Airyscan and LSM880 confocal microscope.

Appendix A. Supplementary data

References

1 F. Reynolds, K.A. Kelly **Techniques for molecular imaging probe design**

Mol. Imaging, 10 (2011), pp. 407-419

2 M. Mahmoudi, V. Serpooshan, S. Laurent **Engineered nanoparticles for biomolecular imaging**

Nanoscale, 3 (2011), pp. 3007-3026

3 C. Corot, P. Robert, J.M. Idée, M. Port **Recent advances in iron oxide nanocrystal technology for medical imaging**

Adv. Drug Deliv. Rev., 58 (2006), pp. 1471-1504

4 Z. Bakhtiary, A.A. Saei, M.J. Hajipour, M. Raoufi, O. Vermesh, M. Mahmoudi **Targeted superparamagnetic iron oxide nanoparticles for early detection of cancer: possibilities and challenges**

Nanomedicine, 12 (2016), pp. 287-307

5 S. Sharifi, H. Seyednejad, S. Laurent, F. Atyabi, A.A. Saei, M. Mahmoudi **Superparamagnetic iron oxide nanoparticles for *in vivo* molecular and cellular imaging**

Contrast Media Mol. Imaging, 10 (2015), pp. 329-355

6.C.A. Pacak, P.E. Hammer, A.A. MacKay, R.P. Dowd, K.R. Wang, A. Masuzawa, B. Sill, J.D.McCully, D.B. Cowan **Superparamagnetic iron oxide nanoparticles function as a long-term, multi-modal imaging label for non-invasive tracking of implanted progenitor cells**

PLoS One, 9 (2014), p. e108695

7 P.I. Soares, I.M. Ferreira, R.A. Igreja, C.M. Novo, J.P. Borges, **Application of hyperthermia for cancer treatment: recent patents review**, Recent Pat. Anticancer Drug Discov. 7 (2012) 64–73.

8 O. Veiseh, J.W. Gunn, M. Zhang **Design and fabrication of magnetic nanoparticles for targeted drug delivery and imaging**

Adv. Drug Deliv. Rev., 62 (2010), pp. 284-304

9
M.G. Shapiro, P.W. Goodwill, A. Neogy, M. Yin, F.S. Foster, D.V. Schaffer, S.M. Conol ly **Biogenic gas nanostructures as ultrasonic molecular reporters**

Nat. Nanotechnol., 9 (2014), pp. 311-316

10.M.G. Shapiro, R.M. Ramirez, L.J. Sperling, G. Sun, J. Sun, A. Pines, D.V. Schaffer, V.S. Bajaj **Genetically encoded reporters for hyperpolarized xenon magnetic resonance imaging**

Nat. Chem., 6 (2014), pp. 629-634

11 D. Schüler **Genetics and cell biology of magnetosome formation in magnetotactic bacteria**

FEMS Microbiol. Rev., 32 (2008), pp. 654-672

12 D. Faivre, D. Schüler **Magnetotactic bacteria and magnetosomes**

Chem. Rev., 108 (2008), pp. 4875-4898

13.Y.W. Jun, Y.M. Huh, J.S. Choi, J.H. Lee, H.T. Song, S. Kim, S. Yoon, K.S. Kim, J.S . Shin, J.S.Suh, J. Cheon **Nanoscale size effect of magnetic nanocrystals and their utilization for cancer diagnosis via magnetic resonance imaging**

J. Am. Chem. Soc., 127 (2005), pp. 5732-5733

14 J. Xie, K. Chen, X. Chen **Production, modification and bio-applications of magnetic nanoparticles gestated by magnetotactic bacteria**

Nano Res., 2 (2009), pp. 261-278

15 Q.L. Vuong, J.F. Berret, J. Fresnais, Y. Gossuin, O. Sandre **A universal scaling law to predict the efficiency of magnetic nanoparticles as MRI T_2-contrast agents**

Adv. Healthc. Mater, 1 (2012), pp. 502-512

16.N. Lee, H. Kim, S.H. Choi, M. Park, D. Kim, H.C. Kim, Y. Choi, S. Lin, B.H. Kim, H. S. Jung, H.Kim, K.S. Park, W.K. Moon, T. Hyeon **Magnetosome-like ferrimagnetic iron oxide nanocubes for highly sensitive MRI of single cells and transplanted pancreatic islets**

Proc. Natl. Acad. Sci. U. S. A, 108 (2011), pp. 2662-2667

17.S. Mériaux, M. Boucher, B. Marty, Y. Lalatonne, S. Prévéral, L. Motte, C.T. Lefèvre, F. Geffroy, F. Lethimonnier, M. Péan, D. Garcia, G. Adryanczyk-Perrier, D. Pignol, N. Ginet **Magnetosomes, biogenic magnetic nanomaterials for brain molecular imaging with 17.2 T MRI scanner**

Adv. Healthc. Mater, 4 (2015), pp. 1076-1083

18 J. Sun, Y. Li, X.J. Liang, P.C. Wang **Bacterial magnetosome: a novel biogenetic magnetic targeted drug carrier with potential multifunctions**

J. Nanomater, 2011 (2011), pp. 469031-469043

19 J. Sun, T. Tang, J. Duan, P.X. Xu, Z. Wang, Y. Zhang, L. Wu, Y. Li **Biocompatibility of bacterial magnetosomes: acute toxicity, immunotoxicity and cytotoxicity**

Nanotoxicology, 4 (2010), pp. 271-283

20.A. Hartunga, M.R. Lisy, K.H. Herrmann, I. Hilger, D. Schüler, C. Lang, M.E. Bellem ann, W.A.Kaiser, J.R. Reichenbach **Labeling of macrophages using bacterial magnetosomes and their characterization by magnetic resonance imaging**

J. Magn. Magn. Mater, 311 (2007), pp. 454-459

21 E. Alphandéry **Applications of magnetosomes synthesized by magnetotactic bacteria in medicine**

Front. Bioeng. Biotechnol., 2 (2014), p. 5

22.T. Orlando, S. Mannucci, E. Fantechi, G. Conti, S. Tambalo, A. Busato, C. Innocent i, L. Ghin, R.Bassi, P. Arosio, F. Orsini, C. Sangregorio, M. Corti, M.F. Casula, P. Marz ola, A. Lascialfari, A.Sbarbati **Characterization of magnetic nanoparticles from *Magnetospirillum Gryphiswaldense* as potential theranostics tools**

Contrast Media Mol. Imaging, 11 (2016), pp. 139-145

23.K. Grünberg, E.C. Müller, A. Otto, R. Reszka, D. Linder, M. Kube, R. Reinhardt, D. Schüler **Biochemical and proteomic analysis of the magnetosome membrane in *Magnetospirillum Gryphiswaldense***

Appl. Environ. Microbiol., 70 (2004), pp. 1040-1050

24.N. Ginet, R. Pardoux, G. Adryanczyk, D. Garcia, C. Brutesco, D. Pignol **Single-step production of a recyclable nanobiocatalyst for organophosphate pesticides biodegradation using functionalized bacterial magnetosomes**

PLoS One, 6 (2011), p. e21442

25.S.C. Baetke, T. Lammers, F. Kiessling **Applications of nanoparticles for diagnosis and therapy of cancer**

Br. J. Radiol., 88 (2015), p. 20150207

26.F. Zhang, X. Huang, L. Zhu, N. Guo, G. Niu, M. Swierczewska, S. Lee, H. Xu, A.Y. Wang, K.A.Mohamedali, M.G. Rosenblum, G. Lu, X. Chen **Noninvasive monitoring of orthotopic glioblastoma therapy response using RGD-conjugated iron oxide nanoparticles**

Biomaterials, 33 (2012), pp. 5414-5422

27.J. Fang, H. Nakamura, H. Maeda **The EPR effect: unique features of tumor blood vessels for drug delivery, factors involved, and limitations and augmentation of the effect**

Adv. Drug Deliv. Rev., 63 (2011), pp. 136-151

28.F. Danhier, A. Le Breton, V. Préat **RGD-based strategies to target alpha(v) beta(3) integrin in cancer therapy and diagnosis**

Mol. Pharm., 9 (2012), pp. 2961-2973

29.P.T. Caswell, J.C. Norman **Integrin trafficking and the control of cell migration**

Traffic, 7 (2006), pp. 14-21

30.P.C. Brooks, R.A. Clark, D.A. Cheresh **Requirement of vascular integrin alpha v beta 3 for angiogenesis**

Science, 264 (1994), pp. 569-571

31.C. Zhang, M. Jugold, E.C. Woenne, T. Lammers, B. Morgenstern, M.M. Mueller, H. Zentgraf, M.Bock, M. Eisenhut, W. Semmler, F. Kiessling **Specific targeting of tumor angiogenesis by RGD-conjugated ultrasmall superparamagnetic iron oxide particles using a clinical 1.5-T magnetic resonance scanner**

Cancer Res., 67 (2007), pp. 1555-1562

32.T. Matsunaga, Y. Okamura, Y. Fukuda, A.T. Wahyudi, Y. Murase, H. Takeyama **Complete genome sequence of the facultative anaerobic magnetotactic bacterium *Magnetospirillum sp.* strain AMB-1**

DNA Res., 12 (2005), pp. 157-166

33.D. Murat, A. Quinlan, H. Vali, A. Komeili **Comprehensive genetic dissection of the magnetosome gene island reveals the step-wise assembly of a prokaryotic organelle**

Proc. Natl. Acad. Sci. U. S. A, 107 (2010), pp. 5593-5598

34.J. Dennie, J.B. Mandeville, J.L. Boxerman, S.D. Packard, B.R. Rosen, R.M. Weissk off **NMR imaging of changes in vascular morphology due to tumor angiogenesis**

Magn. Reson. Med., 40 (1998), pp. 793-799

35 S.S. Stylli, R.B. Luwor, T.M. Ware, F. Tan, A.H. Kaye**Mouse models of glioma**

J. Clin. Neurosci., 22 (2015), pp. 619-626

36
S. Rieken, D. Habermehl, A. Mohr, L. Wuerth, K. Lindel, K. Weber, J. Debus, S.E. Co mbs **Targeting αvβ3 and αvβ5 inhibits photon-induced hypermigration of malignant glioma cells**

Radiat. Oncol., 6 (2011), p. 132

37 S. Hak, J. Cebulla, E.M. Huuse, L. Davies
Cde, W.J. Mulder, H.B. Larsson, O. Haraldseth **Periodicity in tumor vasculature targeting kinetics of ligand-functionalized nanoparticles studied by dynamic contrast enhanced magnetic resonance imaging and intravital microscopy**

Angiogenesis, 17 (2014), pp. 93-107

38. D. Moncelet, V. Bouchaud, P. Mellet, E. Ribot, S. Miraux, J.M. Franconi, P. Voisin **Cellular density effect on RGD ligand internalization in glioblastoma for MRI application**

PLoS One, 8 (2013), p. e82777

39.R.-T. Liu, J. Liu, J.-Q. Tong, T. Tang, W.-C. Kong, X.-W. Wang, Y. Li, J.-
T. Tang**Heating effect and biocompatibility of bacterial magnetosomes as potential materials used in magnetic fluid hyperthermia**

Prog. Nat. Sci., 22 (2012), pp. 31-39

40 L. Xiang, J. Wei, S. Jianbo, W. Guili, G. Feng, L. Ying **Purified and sterilized magnetosomes from Magnetospirillum gryphiswaldense MSR-1 were not toxic to mouse fibroblasts in vitro**

Lett. Appl. Microbiol., 45 (2007), pp. 75-81

41.L. Han, S.Y. Li, Y. Yang, F.M. Zhao, J. Huang, J. Chang **Research on the structure and performance of bacterial magnetic nanoparticles**

J. Biomater. Appl., 22 (2008), pp. 433-448

42.J.A. Kim, H.J. Lee, H.J. Kang, T.H. Park **The targeting of endothelial progenitor cells to a specific location within a microfluidic channel using magnetic nanoparticles**

Biomed. Microdevices, 11 (2009), pp. 287-296

43.L. Yan, X. Yue, S. Zhang, P. Chen, Z. Xu, Y. Li, H. Li **Biocompatibility evaluation of magnetosomes formed by Acidithiobacillus ferrooxidans**

Mater. Sci. Eng. C Mater. Biol. Appl., 32 (2012), pp. 1802-1807

44.C. Chen, P. Wang, L. Li **Applications of bacterial magnetic nanoparticles in nanobiotechnology**

J. Nanosci. Nanotechnol., 16 (2016), pp. 2164-2171

45. E. Alphandéry, S. Faure, O. Seksek, F. Guyot, I. Chebbi **Chains of magnetosomes extracted from AMB-1 magnetotactic bacteria for application in alternative magnetic field cancer therapy**

ACS Nano, 5 (2011), pp. 6279-6296

46.S. Mannucci, L. Ghin, G. Conti, S. Tambalo, A. Lascialfari, T. Orlando, D. Benati, P. Bernardi, N.Betterle, R. Bassi, P. Marzola, A. Sbarbati **Magnetic nanoparticles from *Magnetospirillum Gryphiswaldense* increase the efficacy of thermotherapy in a model of colon carcinoma**

PLoS One, 9 (2014), p. e108959

Supplementary data

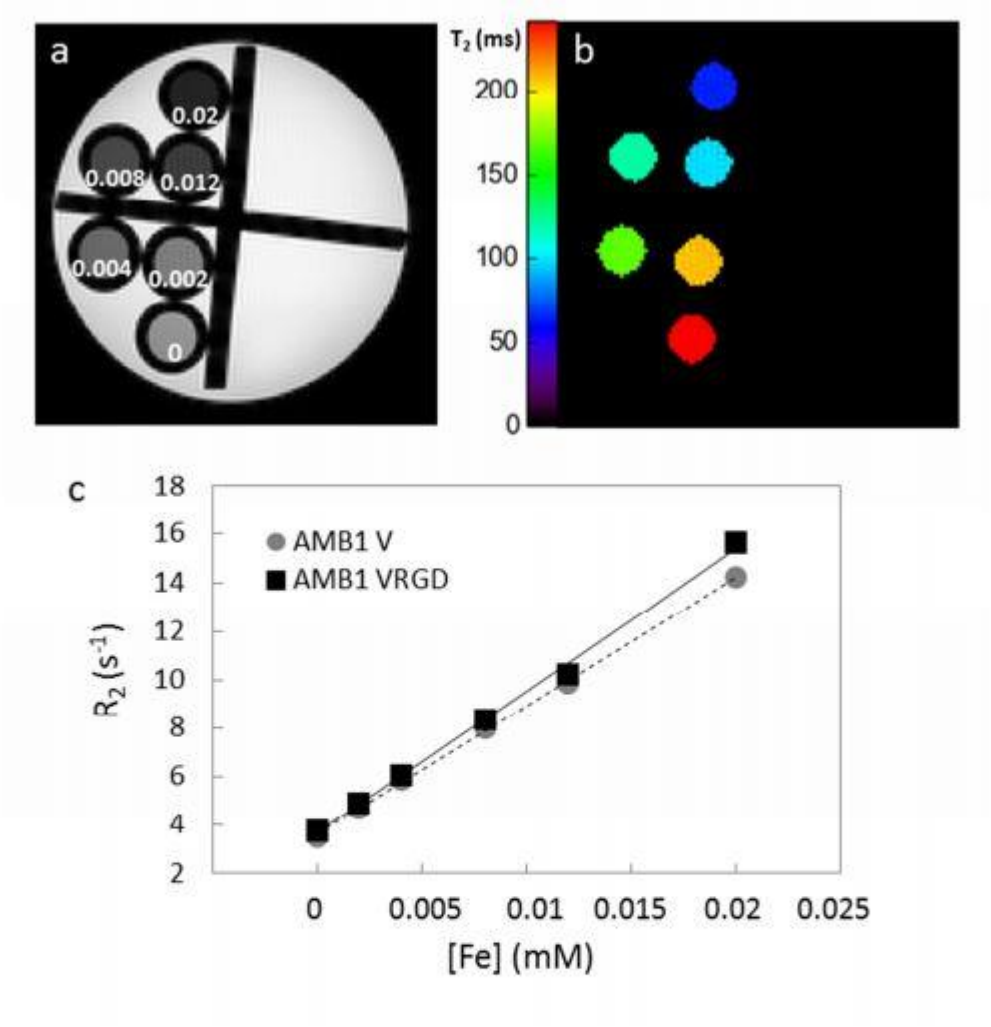

Figure S1: Transverse relaxivity measurements at 11.7 T. a/ T_2-weighted image of a phantom containing several tubes filled with different concentrations of AMB1 VRGD magnetosomes suspended in agar matrix. The higher is magnetosomes concentration, the lower (*i.e.* darker) is the MRI signal (magnetosomes concentration in mM is written in white on each tube). b/ T_2 parametric map reconstructed from the multi-echo acquisition enables to quantify the contrast induced by each magnetosomes concentration. c/ Transverse relaxivity is measured as the slope of the linear fit of the transverse relaxation rate R_2 ($=1/T_2$) versus the iron concentration.

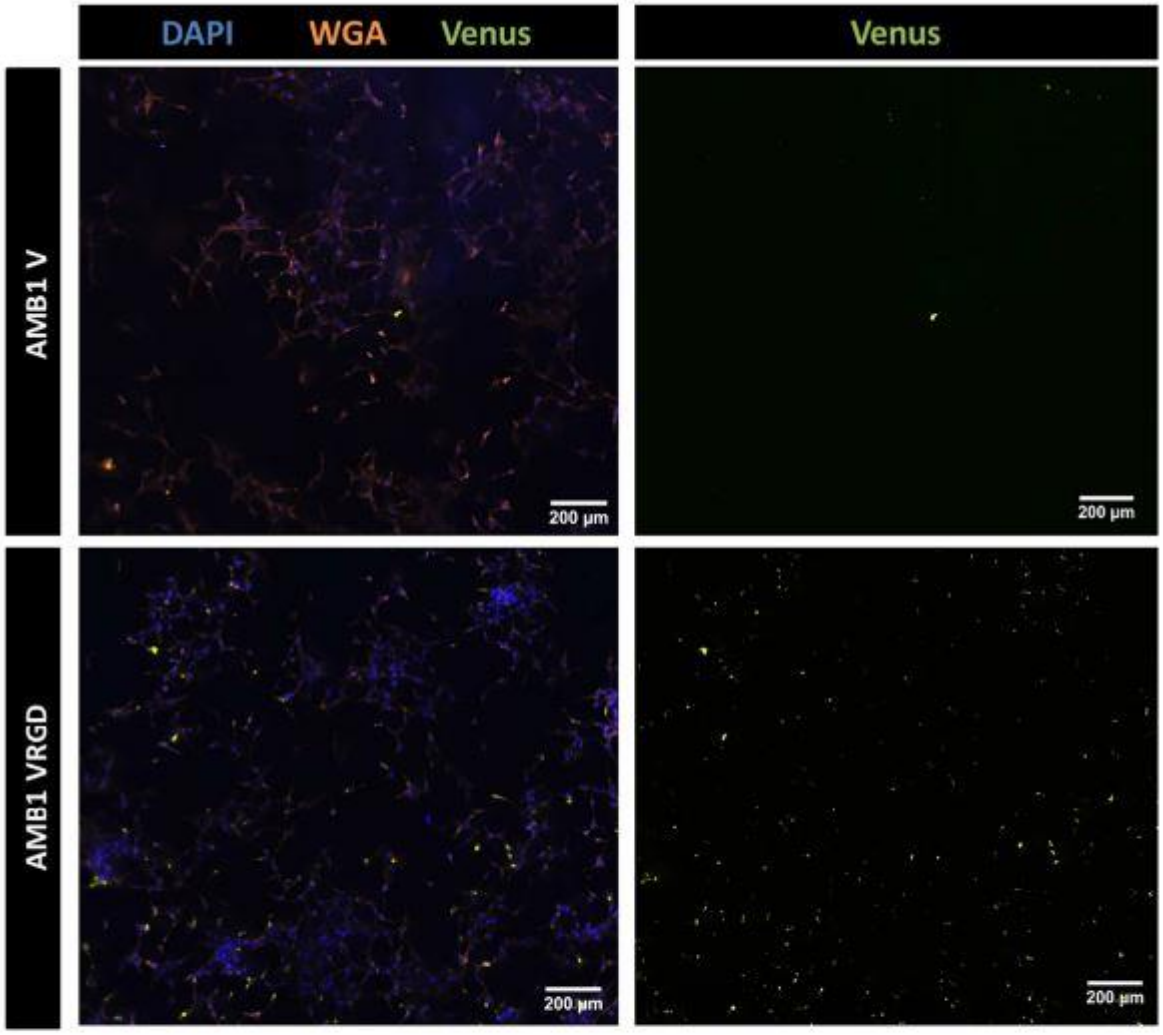

Figure S2: *In vitro* study of AMB1 VRGD affinity to U87 cells. ×20 magnification mosaic images of U87 cells, after 3h30 of incubation with AMB1 V (control) or AMB1 VRGD (2 mg_{Fe}/L), enable the quantification of Venus fluorescence (in green) co-localized with cell membrane (Texas Red, Wheat Germ Agglutinin staining in orange).

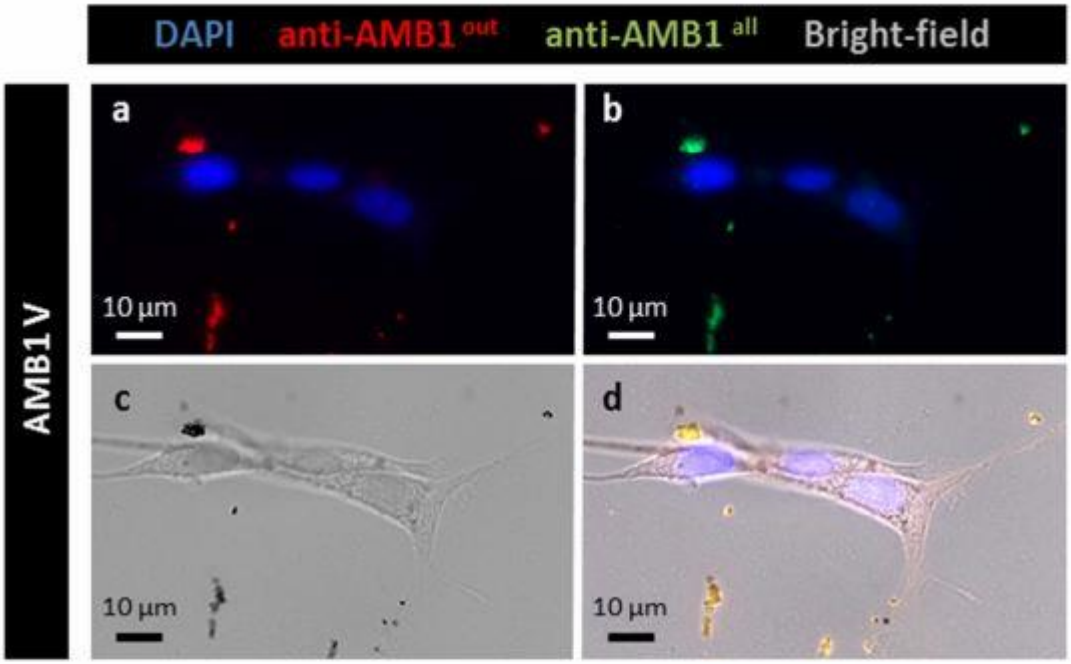

Figure S3: *In vitro* study of AMB1 V internalization inside U87 cells. ×63 magnification fluorescence and bright-field images of U87 cells, after 24h of incubation with AMB1 V (250 μg_{Fe}/L). a/ Merged fluorescence image acquired before detergent treatment shows cell nuclei (DAPI staining in blue) and magnetosomes localized only outside cells (anti-AMB1 staining revealed in red). b/ Merged fluorescence image acquired after detergent treatment shows cell nuclei (DAPI staining in blue) and all magnetosomes (anti-AMB1 staining revealed in green). c/ Bright-field image acquired after detergent treatment shows clusters of iron-oxide crystals. d/ Overlay of previous fluorescence and bright-field images (a,b,c) reveals all magnetosomes in yellow, confirming that they are exclusively localized outside cells.

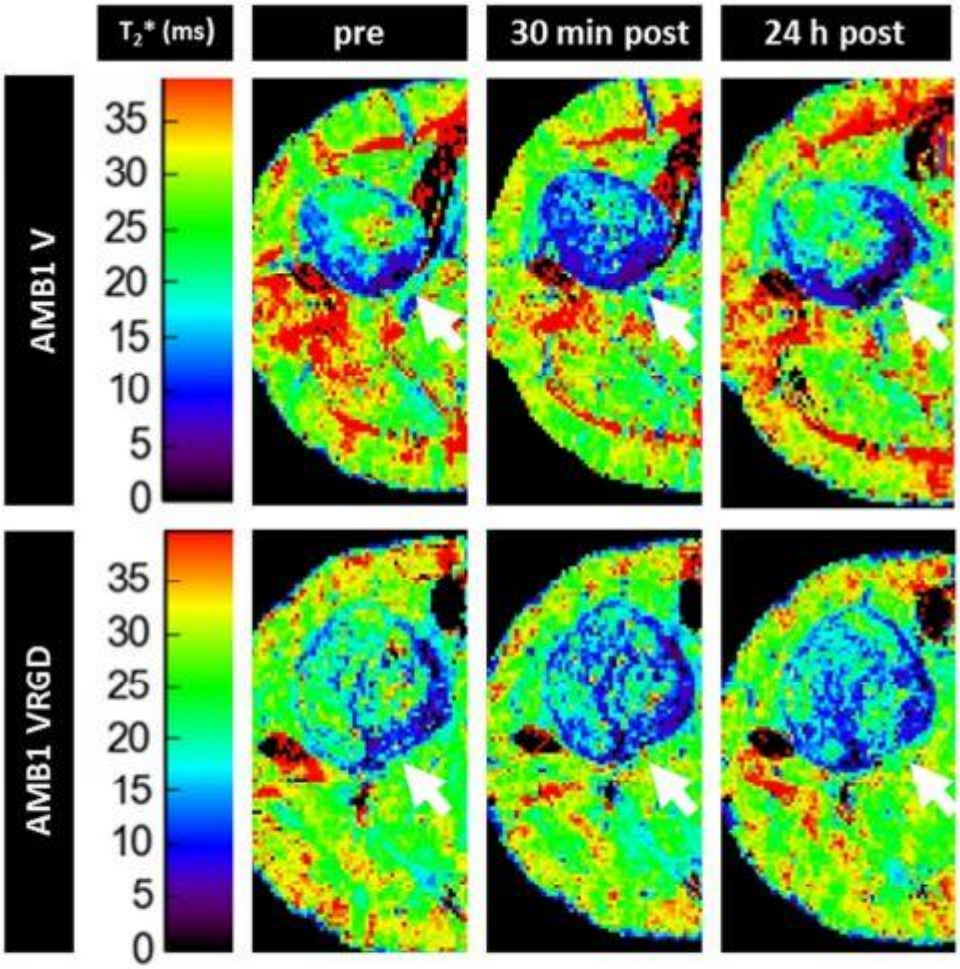

Figure S4: Long-term follow-up of MRI contrast in brain of glioblastoma-bearing mice after injection of functionalized (n = 5) and control (n = 4) magnetosomes. T_2* parametric maps showing tumor area (white arrows), acquired before, 30 min and 24 h after magnetosomes injection.

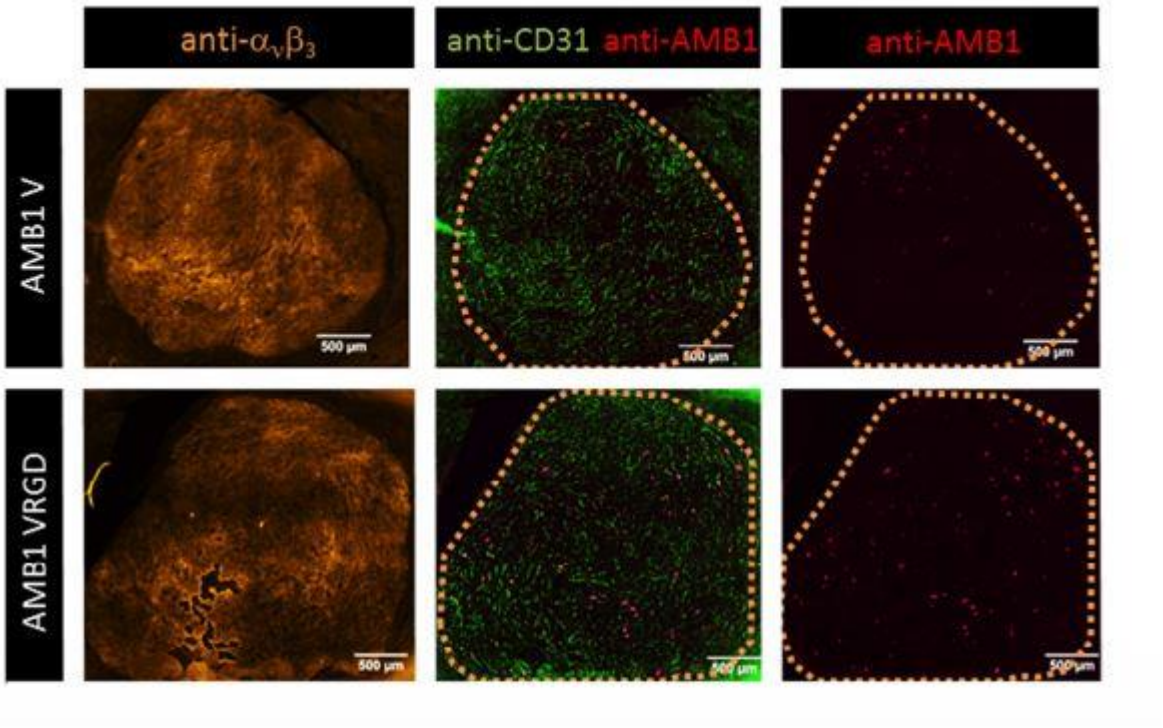

Figure S5: *Post mortem* evaluation of magnetosomes accumulation inside tumor. ×20 magnification mosaic fluorescence images acquired after immunostainings of histological mouse brain slices (20 µm thickness), showing $\alpha_v\beta_3$ integrins (anti-$\alpha_v\beta_3$ staining revealed in orange), vessels (anti-CD31 staining revealed in green) and magnetosomes (anti-AMB1 staining revealed in red). Mice were injected with AMB1 V (upper panels) or AMB1 VRGD (lower panels) magnetosomes. Border of the tumor is delineated thanks to $\alpha_v\beta_3$ orange channel (left images), and plotted in orange dashed lines in the green and red channels for better visualization (middle and right images).